Hindawi
International Journal of Energy Research
Volume 2023, Article ID 6020430, 14 pages
https://doi.org/10.1155/2023/6020430

Research Article

Convection Cooling Enhancement for Energy Conversion Systems Using Rhombic-Dodecahedral-Zeolitic-Imidazolate-Framework-8-Nanotextured Surfaces

Chanwoo Park,[1] Kwangjin Jang,[1] Jungwoo Huh,[1] Bhavana Joshi,[1] Ali Aldalbahi,[2] Mostafizur Rahaman,[2] Chan-Sol Ahn,[3] Boo-Hyoung Bang,[4] and Sam S. Yoon[1]

[1]*School of Mechanical Engineering, Korea University, Seoul 02841, Republic of Korea*
[2]*Department of Chemistry, College of Science, King Saud University, Riyadh 11451, Saudi Arabia*
[3]*Fire Research Center, Korea Institute of Civil Engineering and Building Technology, 283, Goyang-daero, Ilsanseo-gu, 10223 Goyang-si, Republic of Korea*
[4]*Department of Energy Mechanical Engineering, Gyeonggi University of Science and Technology, 269, Gyeonggigwagidae-ro, Siheung-si, 15073, Republic of Korea*

Correspondence should be addressed to Boo-Hyoung Bang; bhbang@gtec.ac.kr and Sam S. Yoon; skyoon@korea.ac.kr

Received 2 May 2023; Revised 17 July 2023; Accepted 29 July 2023; Published 24 August 2023

Academic Editor: Geng Chen

Copyright © 2023 Chanwoo Park et al. This is an open access article distributed under the Creative Commons Attribution License, which permits unrestricted use, distribution, and reproduction in any medium, provided the original work is properly cited.

Evaporative cooling is an efficient approach for removing heat from nuclear reactors, solar power plants, solar panels, and energy storage devices, such as lithium-ion batteries and fuel cells. Nanotextured surfaces can provide improved evaporative cooling by increasing the total surface area to enhance the heat transfer rate and reducing the temperatures of local hotspots. In this study, we introduced rhombic dodecahedral zeolitic imidazolate framework-8 (ZIF8), a class of metal-organic frameworks, via impregnation to create nanotextured surfaces. The impregnation time was varied to obtain various thicknesses of ZIF8. We found that the increased surface area of ZIF8 improved convection cooling, which considerably reduced the temperature of the heated substrate. Air, mist (buoyant aerosols), and spray (inertial droplets) were independently used as coolants to compare the cooling performance of noncoated (bare) and ZIF8-coated substrates. Compared to the noncoated substrate, the optimal ZIF8 film yielded temperature reductions of $\Delta T = 13^{\circ}C$ and $10^{\circ}C$ for air and spray cooling, respectively.

1. Introduction

With the size reduction of energy storage devices, electronic devices, and small modular reactors (SMRs), higher power densities are inevitably generated on the limited surface areas of such devices. As a result, thermal stresses and loads have increased substantially [1–4]. Usually, electronic devices, energy storage devices, or SMRs fail beyond a certain thermal load limit [4–9]. This thermal shutdown of energy conversion systems poses a problem not only for portable devices but also for stationary devices used in the energy sector, including solar panels and solar air heaters. For example, when a solar panel is overheated, the energy conversion efficiency decreases substantially (i.e., a 0.5% decrease in efficiency for every $1^{\circ}C$ increase), and a temperature increase in the range of 10–$40^{\circ}C$ is quite common during hot weather [10, 11]. Solar air heaters, which collect solar radiation, inevitably heat up, and this can induce thermal-driven structural damage. Therefore, local surface temperatures must be reduced by implementing efficient cooling schemes for these devices [12].

Previously, air, mist (buoyant aerosols), spray (inertial droplets), and liquid water have been used for electronic cooling [13, 14]. In general, natural air cooling is adopted to cool solar panels and cellular phones because the use of air is economical. Forced air cooling is generally used for laptops or workstations to cool central processing units. Previously, relatively small buoyant aerosols and mist cooling have been used for both indoor and outdoor cooling. As buoyant aerosols have a relatively small size, they rapidly

evaporate, which leads to a reduction in their surrounding temperatures [15, 16]. Such mist cooling is particularly effective in dry regions, where the saturation pressure of the sprayed droplets is greater than the vapor pressure of the surrounding. Mist and spray cooling have been used in various industrial equipment such as electronics [17], solar chimney [18], nuclear reactors [19], electric vehicles [20], hypersonic transportation [21], and aerospace devices [22].

For electronic cooling, mist or spray cooling must be performed carefully to avoid flooding, which may cause electrical shorts or damage the system. Liquid water is used to cool large thermal systems such as nuclear reactors. However, beyond a temperature limit, film boiling may occur. In this case, cooling may be drastically reduced, and a structural meltdown may occur; an example of this is the *Chernobyl* nuclear accident. To delay film boiling even under extreme superheating conditions, some studies on pool boiling have focused on increasing the critical heat flux (CHF) and effective heat transfer coefficient (h_{eff}). These pool-boiling concepts have been applied to electronic cooling. Electronics that perform heavy computations and transfer massive amounts of data require cooling schemes to prevent overheating. Pool boiling performance is generally assessed by the magnitude of the CHF and h_{eff}, which are predominantly governed by surface roughness and wettability [14].

In general, increasing the surface roughness and wettability is favorable for increasing the cooling efficiency. Theoretically, a rougher surface provides an increased surface area, which increases the overall heat transfer rate. A surface with high wettability is also beneficial for enhancing cooling during spray or water cooling owing to the affinity of water for hydrophilic surfaces, which promotes the interaction between water and the surface. The roughness length scale can be categorized into three regimes: macro, micro, and nanoscale. Among these, the nanoscale roughness is advantageous because it provides the largest surface area. Therefore, numerous nanotexture-based studies have been conducted to increase the magnitude and rate of heat transfer [23–27].

Sinha-Ray et al. [28] introduced metal oxide nanofibers decorated with sharp thorns to increase the overall surface area. The thorny nanofibers were found to be capable of eliminating a heat flux level of the order of a few $\text{kW}\cdot\text{cm}^{-2}$ when using water. An et al. [25] used copper oxide nanofibers to cool a heated plate by natural air cooling and demonstrated a temperature reduction of 7.7°C in the optimal case. Yoon et al. [29] introduced various nanotexturing schemes, including the use of metal oxide nanofibers, silver nanowires, and graphene nanosheets. They concluded that silver nanowires produced the lowest cooling temperature in the water-cooled case. Kim et al. [30] produced a rough copper surface using supersonic spraying and compared its cooling performance with that of other nanotextured surfaces. Kim et al. [31] also used Ni-electroplated nanofibers to cool plates heated in air. The nickel nanofibers were found to be capable of not only reducing the local temperature but also distributing heat over the entire heated surface, effectively reducing the local thermal stress. Kim et al. [32] introduced bismuth vanadate micropillars for air and spray cooling and demonstrated that hydrophilic textured surfaces enhanced the air and spray cooling performances. Thus, nanotextured surfaces have been demonstrated to be an effective means of enhancing convection cooling capability.

Herein, we introduce a nanotextured surface composed of zeolitic imidazolate framework-8 (ZIF8) prepared by supersonic spraying to cool heated surfaces. Notably, ZIF8 belongs to a class of metal-organic frameworks (MOFs) with a unique porous structure [33]. ZIF8 has a topology similar to that of zeolites and consists of tetrahedrally coordinated transition-metal cations interlinked by imidazole-based ligands [34]. ZIF8 has been used in numerous industrial applications, including selective separation membranes, oil–water separation [35], water purification [36–38], gas–vapor separation [39–41], energy storage devices [42], drug delivery materials [43], bone tissue, [44], and antibacterial agents [45]. However, the unique tetrahedral structure of ZIF8 has never been employed to enhance heat transfer.

In this study, the seeding of ZIF8 nanoparticles on a substrate was performed via supersonic spraying, as shown in Figure 1(a). Subsequently, an impregnation method was used to grow the ZIF8 nanoparticles into tetrahedral structures. Once this was accomplished, the substrate was completely nanotextured, which increased the total surface area and enhanced h_{eff}. Note that when the amount of heat flux (q'') supplied to the substrate is constant (i.e., $q'' = h_{\text{eff}} \cdot \Delta T$, where $\Delta T = T_{\text{sub}} - T_{\text{sat}}$), the substrate temperature T_{sub} is expected to decrease owing to an increase in h_{eff}, while the liquid boiling or saturation temperature, T_{sat}, remains fairly constant. In this study, the impregnation time was varied from 1 to 3 h such that the amount of ZIF8 or the degree of nanotexturing could be varied. These textured surfaces were used for both air and mist (or aerosol) cooling, and the corresponding temperature reductions were observed via parametric studies. Notably, all the cooling scenarios were based on buoyancy-driven natural convection.

2. Experimental

2.1. Deposition of ZIF8. ZIF8 synthesis was initiated by a seeding process in which ZnO particles were first coated onto a copper substrate via supersonic spraying; this was a simple and rapid deposition method. First, 0.2 g of ZnO (Sigma-Aldrich, USA) was mixed in 50 ml of *N*,*N*-dimethylformamide (DMF; anhydrous, 99.8%, Sigma-Aldrich, USA) with 0.3 ml of 8 wt% polyacrylonitrile (PAN, Mw 150,000, Sigma-Aldrich, USA). The resulting solution was magnetically stirred (PC-420D; Corning Corp., USA) for 10 min and then supersonically sprayed onto a copper substrate.

The supersonic spray coating equipment (Figure 1(a)) consisted of a converging–diverging (de Laval) nozzle, an atomizer (VCX134, Sonics & Materials Inc., USA), an air-gas compressor, an air heater (F076250, Joowonheater, Republic of Korea), a syringe pump (Legato210, KD Scientific Inc., USA), and an *X*–*Y* moving stage (DRMC 140, Mncautomation Inc., Republic of Korea). The ZnO solution was supplied directly to the atomizer using a syringe pump at a flow rate of $1.5\,\text{ml}\cdot\text{min}^{-1}$. The ZnO solution was first

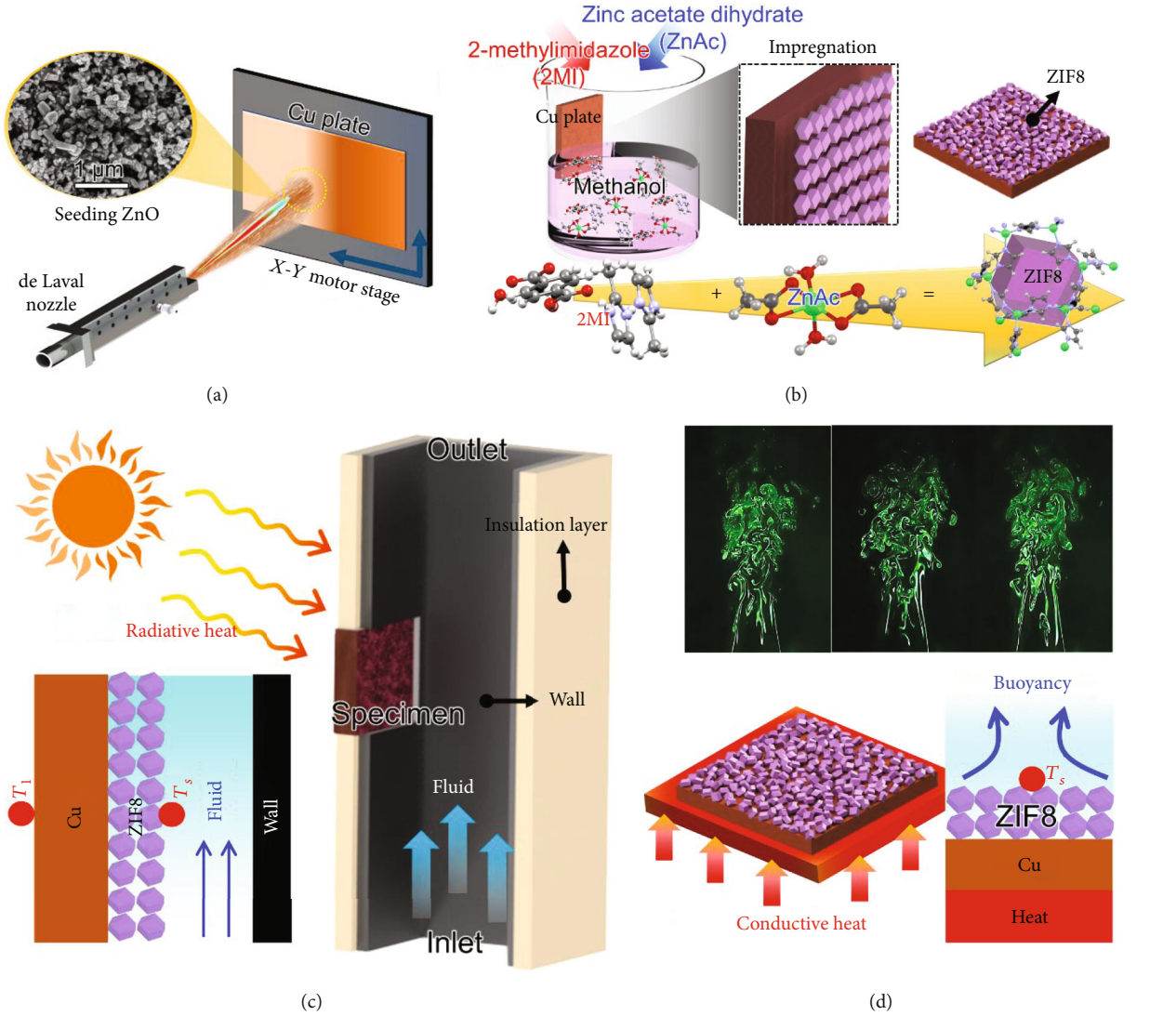

Figure 1: (a) Schematic of the supersonic spray coating process for seeding ZnO particles. (b) ZIF8 growth via impregnation. (c) Buoyant air or mist flow inside the vertical channel attached to a solar collector (i.e., substrate) coated with a ZIF8 layer. (d) Visualization of natural convection cooling over a heated copper substrate coated with ZIF8.

atomized and then injected into a supersonic air stream. Compressed air was heated to 250°C by the air heater and passed through a de Laval nozzle to expand the air stream to a supersonic state. Typically, ZnO solutions vaporize quickly when exposed to hot-air streams. For our analysis, the nozzle-to-substrate distance was set to 15 cm, which provided sufficient travel time for the atomized droplets to evaporate such that only solid ZnO particles remained at the instant of impact.

Figure 1(b) illustrates the impregnation method used to grow the ZIF8 particles on a ZnO-seeded copper substrate (seeded using supersonic spraying). The ZnO-seeded copper plate was immersed in a mixture of 2.4 mM 2-methylimidazole (2MI, Sigma-Aldrich, USA) and 0.6 mM zinc acetate dihydrate (ZnAc, ACS reagent, ≥99.0% (KT), Sigma-Aldrich, USA) in 50 ml of methanol. The opposite side of the copper plate was covered with a polyimide tape so that only the seeded side grew into full-scale ZIF8 particles. During the impregnation process, the 2MI/ZnAc solution was continuously stirred at 150 rpm using a magnetic stirrer, and the solution temperature was maintained at 40°C. The impregnation process was performed for 1 and 3 h at 40°C, completely covering the copper plate. Finally, the polyimide tape was removed, and the ZIF8 sample was dried on a plate heater at 45°C for 1 h.

2.2. Air and Mist Cooling during Radiation Heating. Figure 1(c) shows the vertical channel (5 cm × 5 cm × 18 cm) through which air or mist ascended due to buoyancy. The vertical channel was constructed using a 3D printer (Single Plus 3DP-210F; Cubicon Inc., Republic of Korea) with acrylonitrile butadiene styrene (ABSk Filament, Cubicon, Republic of Korea) as a stacking material. A hollow frame was spread at the center of the channel to locate the specimen composed of the ZIF8-coated copper plate. A halogen lamp (solar simulator; ENH-93506, OSRAM, Germany) attached to the vertical

Table 1: List of equipment for heat transfer experiments.

Function	Air & mist cooling	Spray cooling	Conduction
Heat source	Halogen lamp	Ceramic heater	
Radiative heat flux	Solar power meter		—
Surface temperature		Thermocouple	
Data recorder		Data logger	
IR image	—	Thermal imaging infrared camera	—
Visualization	—	—	Diode-pumped solid-state laser
Voltage supply	—	Power supply	

channel was used to irradiate the specimen (3 cm × 3 cm). A solar meter (TM-751, Tenmars Corp., Taiwan) was used to maintain a radiative heat flux of 4003 W/m^2 at the specimen location. A thermocouple (K-type, Omega Inc., Switzerland) with dimensions of 1 mm × 150 mm and a data logger (GL-240, Graphetec, Japan) were used to measure the surface temperature (T_s). The vertical channel was thermally insulated using glass wool to conserve the amount of heat transferred through the specimen; however, perfect insulation was not achieved. Each case was tested for 30 min to achieve a steady state in which the temperature change remained within a standard deviation magnitude of less than 5%.

2.3. Natural Air Cooling during Conduction Heating. Figure 1(d) shows the experimental setup adopted for natural air cooling. The ZIF8-coated copper substrate was placed on a 4 cm × 4 cm ceramic heater (XH-RJ4040, XH, China). Three thermocouples with a probe size of 1 × 150 mm and an uncertainty level of ±0.5°C were installed at the edge and center of the specimen (3 cm × 3 cm). Data were recorded using a data logger (GL-240; Graphetect, USA). Note that the surface temperature (T_s) represents the averaged value of the data collected from the three thermocouples. All the experimental runs lasted for 30 min to allow T_s to approach the steady state. A diode-pumped solid-state laser (532 nm, TEMoo mode, stability <1%) and a polyvinyl chloride plate laser traversing with a responsiveness of 10 Hz were used to visualize buoyant air motion during natural cooling. Table 1 lists the details of the experimental equipment used in the air and mist cooling test and the conduction test introduced in Sections 2.2 and 2.3.

2.4. Characterizations. The morphology of the textured surface was characterized using field-emission scanning electron microscopy (FE-SEM; S-5200, Hitachi, Ltd., Japan), and the average surface roughness and 3D surface morphology profiles were acquired using atomic force microscopy (AFM; XE-7, Park Systems, Republic of Korea). X-ray diffraction (XRD; SmartLab, Rigaku, Japan) in a 2θ range of 5°–80° was conducted at a speed of 0.5° min^{-1} to characterize the crystallinity of the specimens based on Cu-Kα radiation. X-ray photoelectron spectroscopy (XPS) was performed using an X-tool (ULVAC-PHI, Tokyo, Japan) to determine the material content. The static water contact angle (SWCA) was observed using a high-speed camera (Phantom 9.1, Vision Research Inc., USA) and image-processing software (I'MEASURE 3.0, ING PULS, Republic of Korea).

3. Results and Discussion

3.1. Surface Morphology. Figure 2 shows the SEM and 3D profiler images of the noncoated (or bare), ZIF8/1 h, and ZIF8/3 h samples. The bare case represents a copper surface. The ZIF8 films had a uniform distribution of ZIF8 nanoparticles with a rhombic dodecahedral structure, as shown in Figures 2(b) and 2(c). Successful impregnation was confirmed by the rhombic dodecahedral structure of ZIF8 that was well adhered to the copper surface. The degree of texturing substantially increased after ZIF8 growth, providing a much larger surface area than that of the bare case. However, the surface texturing increased only slightly from ZIF8/1 h to ZIF8/3 h. The 3D profile data indicated that the surface roughness increased substantially from the bare sample to the ZIF8/1 h sample: R_a increased from 207 to 336 nm. However, the change in roughness appeared to be minor when comparing the ZIF8/1 h sample to the ZIF8/3 h sample. Therefore, an increase in the impregnation time (from 1 to 3 h) did not substantially increase the surface area because the ZIF8 growth was saturated by 1 h of impregnation.

3.2. XRD and XPS. The crystal structure of the ZIF8-coated Cu plate (ZIF8/3 h) was analyzed using XRD. The XRD pattern displayed in Figure 3(a) show peaks at lower diffraction angles of 5°-20°, confirming the formation of ZIF8 rhombic dodecahedral particles. The magnified XRD spectra (5°–20°) displayed in Figure 3(b) show peaks at $2\theta = 7.3°$, 10.3°, 12.7°, 14.6°, 16.5°, and 18° corresponding to the (110), (200), (211), (220), (310), and (222) planes of ZIF8, respectively [46, 47]. The sharp and consistent XRD peaks related to ZIF8 confirm that the synthesis duration of 3 h does not modify the ZIF8 crystalline structure [48]. The diffraction pattern of the porous structure also confirms the excellent crystallinity of the sodalite structure of ZIF8 [49]. The sharp and dominant peaks apparent in Figure 3(a) at $2\theta = 43.3°$, 50.5°, and 74.2° can be, respectively, indexed to the (111), (200), and (220) planes of Cu (JCPDS 04-0836) and originate from the Cu plate used as the substrate [50]. The other peaks visible in Figure 3(a) at $2\theta = 31.8°$, 34.4°, 36.3°, 47.5°, 56.6°, 62.9°, and 68° can be attributed to the (100), (002), (101), (102), (110), (103), and (112) planes of ZnO, respectively [51, 52]. The

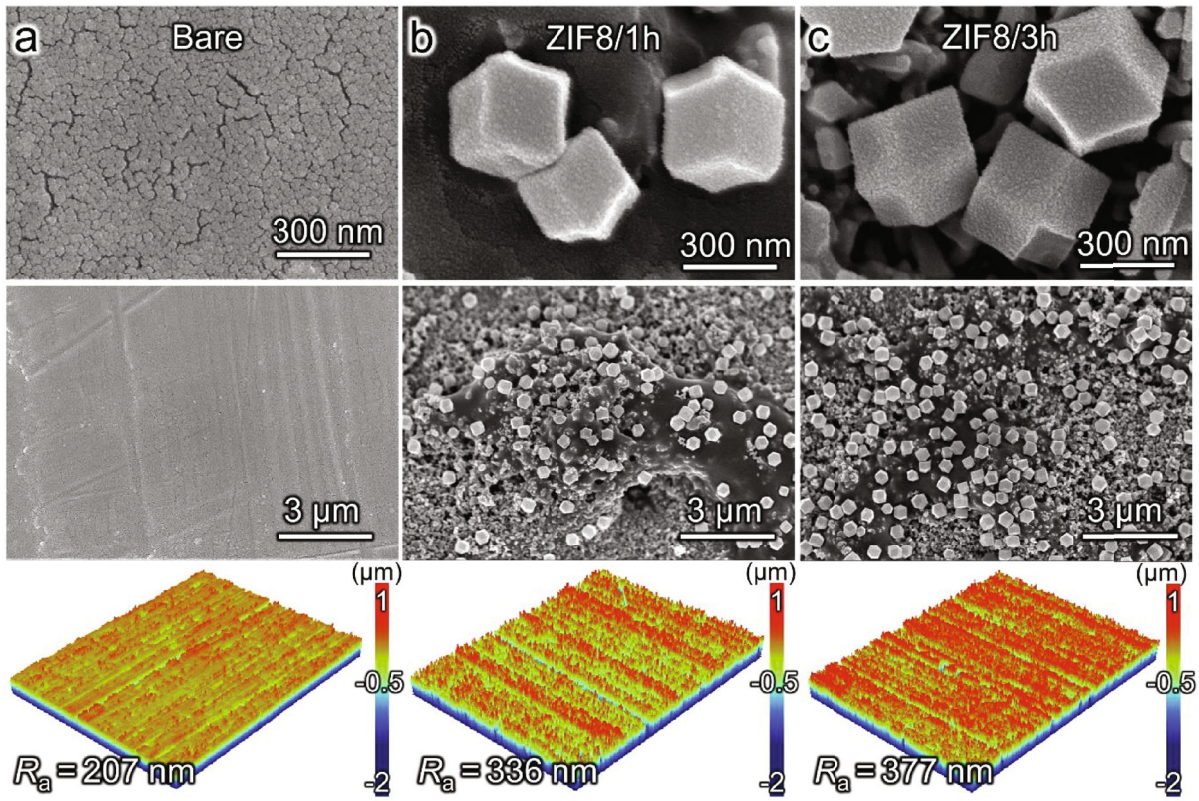

Figure 2: High-magnification SEM (top), low-magnification SEM (middle), and 3D profiler images (bottom) of (a) bare, (b) ZIF8/1 h, and (c) ZIF8/3 h films.

presence of these ZnO peaks can be attributed to the use of ZnO as the seeding material for the ZIF8 coatings. The ZnO particles were observed in the SEM images (Figure 2(c)) after ZIF8 formation, owing to the controlled concentration of imidazolate and the synthesis duration (3 h). In this study, Zn^{2+} ions from zinc acetate and ZnO seeding were utilized to form ZIF8. These Zn^{2+} ions reacted with the imidazolium ions from 2MI via nitrogen to form a rhombohedral shape. In addition, ZnO seeding ensured the excellent adhesion of ZIF8.

The XPS survey spectrum displayed in Figure 3(c) indicates the presence of Zn, O, C, and N in the ZIF8-coated sample [53]. The core spectrum of Zn 2p in Figure 3(d) shows peaks at 1021.82 and 1044.93 eV, corresponding to Zn $2p_{3/2}$ and Zn $2p_{1/2}$, respectively [54]. The binding energy difference between these two Zn 2p peaks is 23.11 eV, confirming the +2 oxidation state of Zn. The O1s peak at 531.9 eV can be deconvoluted in three peaks (Figure 3(e)) at binding energies of 530.7, 531.7, 532.5 eV, indicating the presence of Zn–O attributed to the ZnO-seeded layer, and C–O and Zn–OH in ZIF8. The higher intensity of the peak corresponding to Zn–OH could be attributed to the nanosize of ZIF8, which was beneficial for heat dissipation [55, 56]. Figure 3(f) presents a predominantly narrow C1s spectrum at approximately 286 eV. The deconvolution indicates the presence of three peaks at 284, 285.2, and 286.2 eV attributed to C=C, C–C, and C–N bonding in the imidazole of ZIF8, respectively. The peak in the N1s spectra at 399.06 eV (not shown) was attributed to the pyrrolic imidazole group of the ZIF8 particles [55]. The deconvolution of O1s, C1s, and N1s reflects the formation of ZIF8 using ZnO seeding. The formation of ZIF8 was consistent with the XRD results.

3.3. Air and Mist Cooling. Figures 4(a)–4(c) compare surface temperature (T_s) time plots and convective heat transfer coefficients in the air and mist cooling cases using the bare, ZIF8/1 h, and ZIF8/3 h samples. Figures S1a and S1b confirm that the coated ZIF8 layers were stable and resilient mechanically and thermally while exhibiting the same magnitude of the surface temperature (T_s) throughout the duration of 30 min of convective cooling. Figure 4(d) shows photographs of the experimental setups and the relevant schematics for both the air and mist cooling scenarios. A halogen lamp mimicked solar heat and radiated a heat flux of q''~4000 W·m^{-2}, which was recorded by the solar radiation measurement device (TM-751, Tenmars Corp., Taiwan) at a distance of 13.5 cm from the lamp; note that this is the location where the radiated Cu plate (3 cm × 3 cm) was exposed to the lamp light. The heating power of the lamp was adjusted so that the air temperature on the inner side of the bare sample inside the channel was approximately $T_s = 59.6^{\circ}$C (see the black line in Figure 4(a)), while the temperature on the irradiated side outside the channel was approximately $T_1 = 65^{\circ}$C in

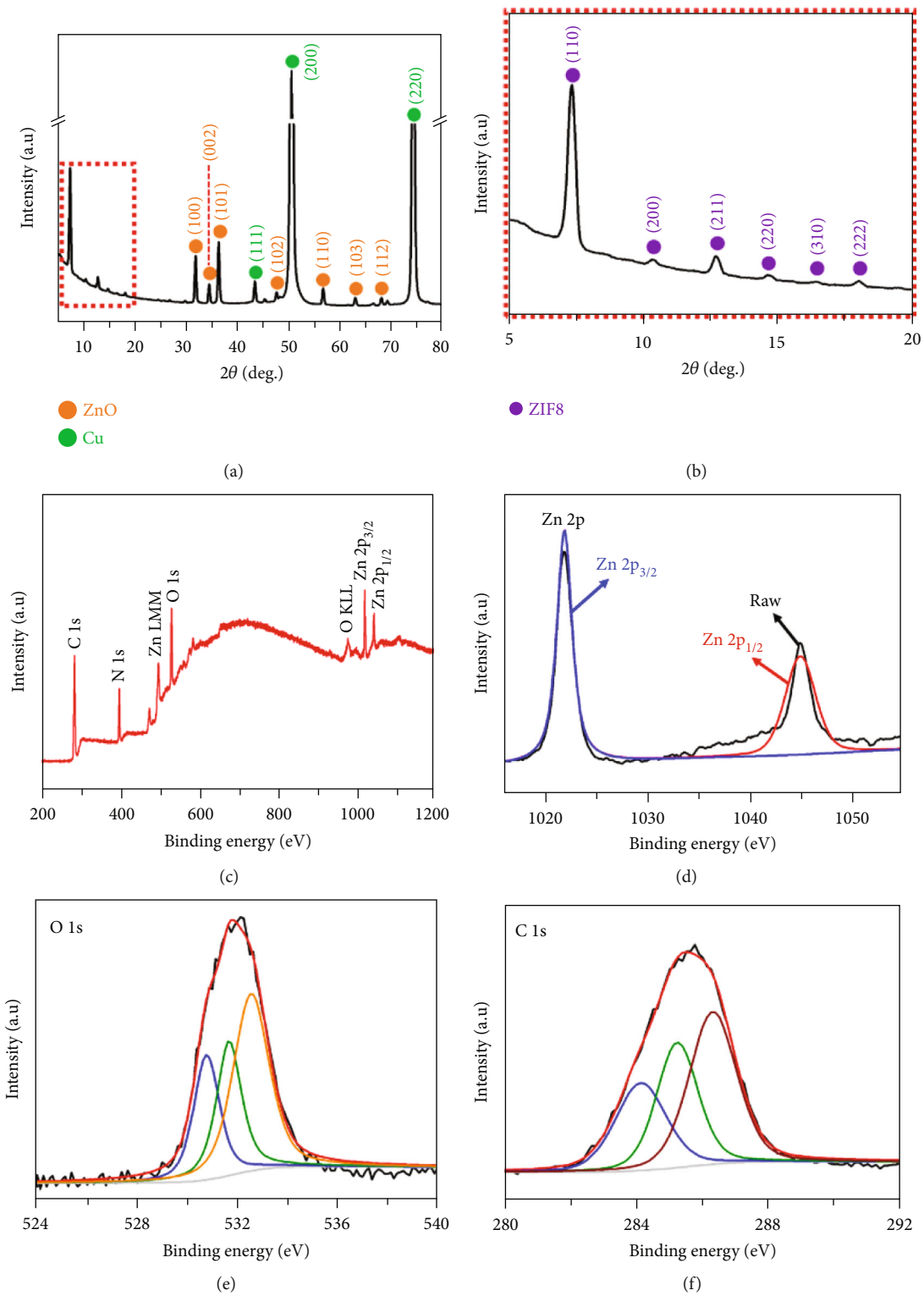

Figure 3: (a) XRD pattern and (b) their magnified views, and (c) XPS spectra of the ZIF8/1 h case. The core spectra of (d) Zn 2p, (e) O1s, and (f) C1s.

the steady state. Notably, the entire surface of the vertical flow channel was thermally insulated using glass fiber, except for the copper substrate depicted with a dashed line in Figure 4(d). Consequently, the copper substrate area was the only heat transfer medium in this experimental setup. In particular, a Fourier conduction model approximation of two layers (i.e., the Cu plate and the ZIF8 layer) yields the following:

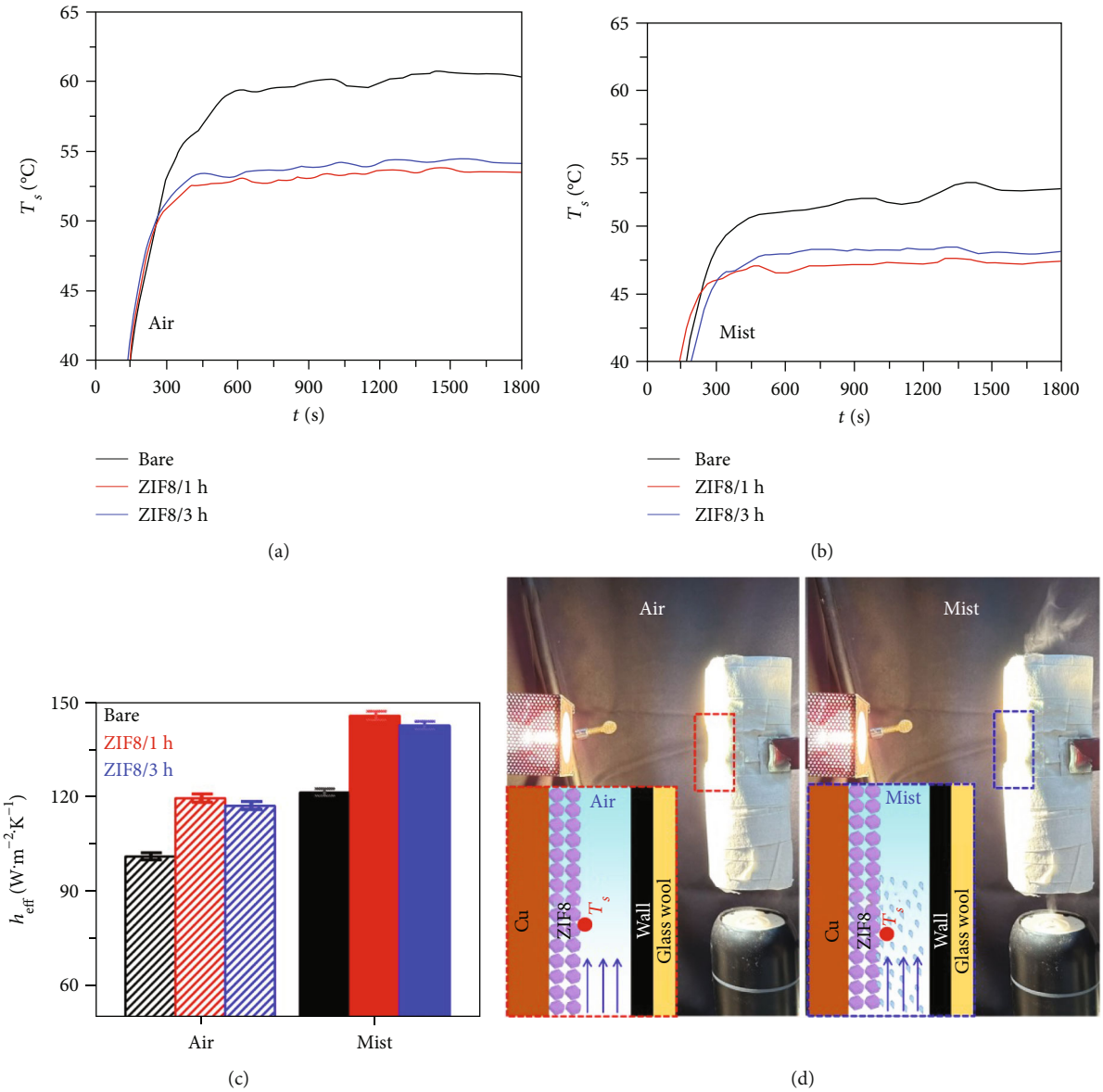

FIGURE 4: Surface temperature-time plots for the bare, ZIF8/1 h, and ZIF8/3 h cases during (a) air and (b) mist cooling, and (c) the corresponding h_{eff}. (d) Photographs and schematic (inset) showing air (left) and mist (right) cooling.

$$q'' = \frac{T_1 - T_s}{(\Delta x/k)_{Cu} + (\Delta x/k)_{ZIF8}}, \quad (1)$$

where k_{Cu} and k_{ZIF8} denote the thermal conductivities of the Cu plate and the ZIF8 layer, respectively. Their thicknesses are $\Delta x_{Cu} = 1$ mm and $\Delta x_{ZIF8} \leq = 1\,\mu$m, respectively. It is noteworthy that Equation (1) assumes that the media are perfectly insulated; thus, heat is transferred only in one direction. Using $T_s = 59.6$°C (see Figure 4(a)), $T_1 = 65$°C, and $k_{Cu} = 400$ W·m^{-1}·K^{-1}, k_{ZIF8} can be calculated to be approximately 0.00073 W·m^{-1}·K^{-1}, which essentially represents a thermal insulator. In this approximation, the copper layer did not significantly affect the temperature change of $\Delta T = T_1 - T_s = 5.4$°C, which was predominantly affected by the presence of the ZIF8-coated layer. In other words, ΔT would have approached zero without the ZIF8-coated layer because of the high thermal conductivity of copper. If the copper-ZIF8 layers were not perfectly insulated, a large portion of the heat collected at the irradiated side would have been transferred along the lateral direction because the ZIF8-layer was a good thermal insulator. Consequently, this scenario invalidated the applicability of Equation (1) in the current case, and only a fraction of the heat received is transferred through the coated area inside the channel. It should also be noted that despite all these imperfections, heat was transferred through the coated side via various routes, and the effect of the ZIF8 coating on cooling was manifested during both air and mist cooling, as shown in Figures 4(a) and 4(b). Figure 4(a) indicates that the inner surface temperature (T_s) of the coated samples was reduced compared to that of the

bare sample during air cooling. The difference between the T_s values of ZIF8/1 h and ZIF8/3 h was negligible because their surface morphologies and areas were nearly identical (see Figures 2(b) and 2(c)). A similar pattern was observed for the mist-cooling scenario, as shown in Figure 4(b). The only difference was that the magnitude of T_s in the mist-cooling scenario was much lower than that in the air-cooling scenario because buoyant liquid aerosols are known to be capable of eliminating heat more efficiently by utilizing the heat of vaporization. It should be noted that the heat of vaporization of water is 2260 kJ/kg, which is far greater than that of any other liquid type, except for liquid iron and aluminum.

In Figure 4(c), the effective convective heat transfer coefficients (h_{eff}) of all cases are presented and compared using Newton's convection equation.

$$h_{\text{eff}} = \frac{q''}{T_s - T_\infty}, \tag{2}$$

where q'' is the heat flux provided to the bare and ZIF8 films. Figure 4(c) compares the values of h_{eff} of the bare and ZIF8 films with a given heat flux of $q'' = 4000\ \text{W·cm}^{-2}$ and an atmospheric temperature of $T\infty = 20^\circ\text{C}$. The h_{eff} values were in the range of $101.1 \le h_{\text{eff}} \le 119.5\ \text{W·m}^2\text{·K}^{-1}$ for the ZIF8-coated layers for air cooling. These h_{eff} values indicate an increase of approximately 18.2% in the cooling efficiency compared with the noncoated (or bare) case. For mist cooling, the h_{eff} range was $121.3 \le h_{\text{eff}} \le 145.5\ \text{W·m}^2\text{·K}^{-1}$ for the coated surfaces. This h_{eff} range was larger than that in the air-cooling scenario. However, we must note that the values of h_{eff} shown in Figure 4(c) may have been overestimated. In the actual case, a nonnegligible amount of heat was transferred to the sidewalls of the Cu plate. As mentioned previously, this heat transfer to the sidewalls is highly likely, particularly when the ZIF8 layer acts as a poor thermal conductor because it is an MOF compound. Heat was diverted to the sidewall because of the hindrance created by the porous ZIF8 layer. Hence, the actual amount of heat provided was substantially smaller than that measured using the solar radiation measurement device. Because the actual heat flux was not known, an overestimated heat flux ($q'' \sim 4000\ \text{W·m}^{-2}$) was utilized to estimate h_{eff}. Although the absolute value of h_{eff} was inaccurate, the relative comparison presented in Figure 4(c) is valid. The h_{eff} values of the ZIF8-coated films are higher than those of the bare film.

Figure 5(a) shows the experimental setup utilized for the natural convection scenario. A ZIF8-coated copper substrate was attached horizontally to a plate heater, and a buoyancy-driven flow was induced during plate heating. As shown in Figures 5(b) and 5(c), the plate heater temperatures were set to $T_h = 100$ and 200°C, respectively, and the corresponding buoyant flow was induced and visualized using incense smoke and laser equipment (532 nm, TEMoo mode, stability <1%). As indicated, the higher-temperature case involved more intense vortical flows, as it entrained a greater amount of flow from the surroundings at the bottom of the plate. Overall, the amount of smoke was larger, and more turbulence was generated when the plate temperature was higher. Figure 5(c) compares the surface temperatures, T_s, measured at the top surfaces of the ZIF8 film during plate heating. Notably, T_h was generally slightly higher than T_s because T_s was measured in the cooling case. Furthermore, plate heating tests were conducted at various bare T_h values of 104.5 and 157.2°C, which correspond to $T_s = 100$ and 150°C, respectively. Figure 5(d) compares the reduction in T_s when changing from the bare to ZIF8-coated cases. As expected, little difference was observed between the ZIF8/1 h and ZIF8/3 h cases; however, the corresponding reductions in T_s were 11 and 16°C with respect to those for the bare case in the $T_s = 100$ and 150°C scenarios, respectively. The ZIF8-coated cases consistently resulted in greater cooling compared to the bare case. In addition, the percentage reductions in T_s with respect to bare T_s were 11 and 10.7%, respectively. This slight change in the percentage reduction confirmed that the cooling effect via texturing was consistent over all temperature ranges.

Figure 5(e) compares the effective heat transfer coefficients, h_{eff}, of the bare, ZIF8/1 h, and ZIF8/3 h cases, which involved heater temperatures of $T_h = 104.5$ and 157.2°C (which correspond to $T_s = 100$ and 150°C, respectively) with an error margin of 2%. Notably, at a higher heater temperature, higher power was required, and the corresponding T_s was also higher. According to Equation (2), h_{eff} is proportional to $q''/(T_s - T_\infty)$ and remains constant for the same material. For example, the h_{eff} values of the bare, ZIF8/1 h, and ZIF8/3 h samples remained fairly constant at various heating temperatures (Figure 5(e)). These values of h_{eff} were estimated using $h_{\text{eff}} = q_h/A_p/(T_s - T_\infty)$, where q_h denotes the heat supplied to the plate heater, T_∞ is the atmospheric temperature ($T_\infty = 20^\circ\text{C}$), and A_p is the projected area of the sample ($A_p = 3\ \text{cm} \times 3\ \text{cm}$). The heat provided can be modelled as follows [57]:

$$q_h = h_h \cdot A_h \cdot (T_h - T_\infty), \tag{3}$$

where h_h is the heat transfer coefficient of the plate heater, A_h represents the surface area of the plate heater ($A_h = 4\ \text{cm} \times 4\ \text{cm}$), and T_h indicates the plate heater temperature ($T_h = 104.5$ and 157.2°C). Generally, the heating plate temperature is higher than the top surface temperature of the substrate ($T_h > T_s$). However, T_s can be equal to T_h for extremely thin foils. The current case had a sufficiently thick substrate, resulting in $T_h > T_s$. The convective heat transfer coefficient of the heater h_h can be estimated using the Nusselt and Grashof numbers as follows [25, 26, 57]:

$$h_h = \frac{k_{\text{air}} \cdot \text{Nu}}{L}, \text{where Nu} = 0.54 \cdot (\text{Gr} \times \text{Pr})^{1/4}, \quad \text{Gr} = \frac{g\beta(T_h - T_\infty)L^3}{\nu^2}. \tag{4}$$

Here, $\beta = 1/T_f$, where $T_f = (T_h + T_\infty)/2$ (i.e., T_f=335 and 362 K). Notably, the thermal conductivity of air at T_f is $k_{\text{air}} = 0.0257\ \text{W·m}^{-1}\text{·K}^{-1}$, and the air Prandtl number ($\text{Pr} = \nu/\alpha$), which is the ratio of momentum diffusivity to

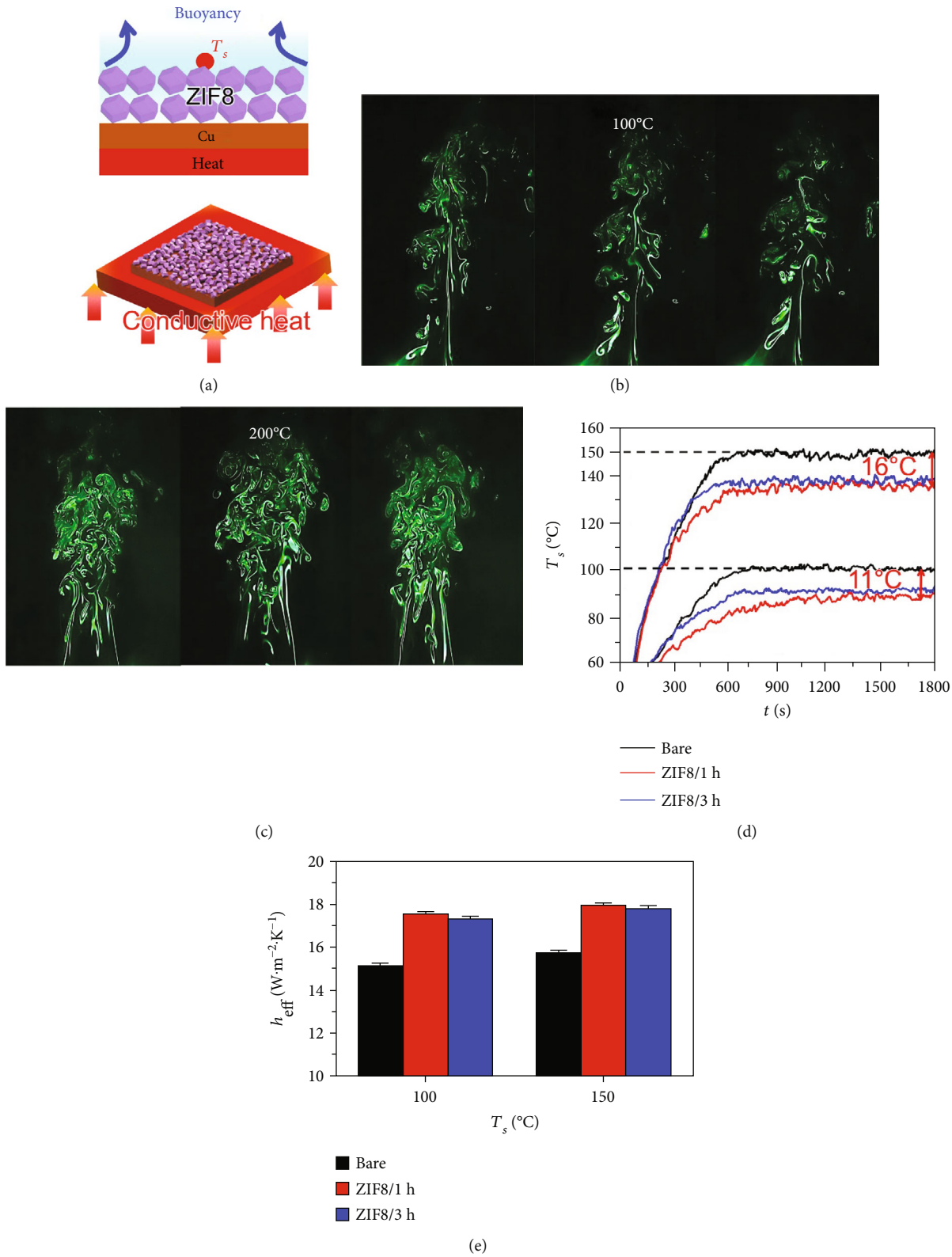

FIGURE 5: (a) Schematic of the natural convection cooling of the ZIF8-coated copper substrate. A photograph showing ascending smoke over the heated ZIF8 film at (b) $T_h = 100^{\circ}C$ and (c) $200^{\circ}C$. (d) Surface temperature of the bare, ZIF8/1 h, and ZIF8/3 h cases at $T_s = 100$ and $150^{\circ}C$. (e) Effective heat transfer coefficients, h_{eff}, corresponding to (a).

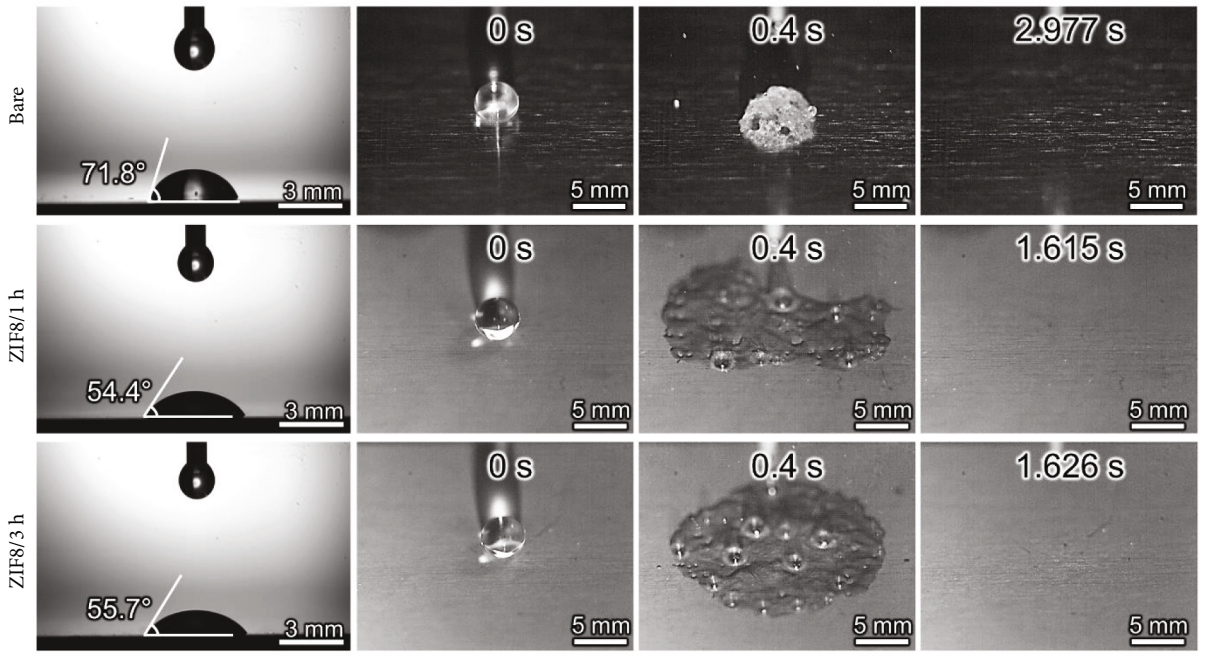

FIGURE 6: Photographs of impacting drops spreading on the bare, ZIF8/1 h, and ZIF8/3 h substrate at $T_{sub} = 140^{\circ}C$ and $H = 1$ cm. The initial diameter of the released drop was $D_0 = 2R_0 = 4.2$ mm.

thermal diffusivity in a laminar flow at T_f, is Pr = 0.7. The kinematic viscosities of air at $T_f = 335$ and 362 K are $\nu = 19.41 \times 10^{-6}$ and 22.24×10^{-6} $m^2 \cdot s^{-1}$, respectively. The corresponding Grashof numbers are Gr = 420,349 and 481,088, respectively. The corresponding Nusselt numbers are Nu = 12.57 and 13.01, respectively. Using Equation (4), the corresponding convective heat transfer coefficients of the heater are determined to be $h_h = 8.08$ and 8.36 $W \cdot m^{-2} \cdot K^{-1}$, respectively. The corresponding heat supplied to the plate heater was estimated using Equation (3): $q_h = 1.09$ and 1.84 W. For the ZIF8/1 h sample, the effective convective heat transfer coefficients were $h_{eff} = q_h/A_p/(T_s T_\infty) = 17.55$ and 17.93 $W \cdot m^{-2} \cdot K^{-1}$, corresponding to $T_s = 89$ and 134°C, respectively (see Figure 5(e)). Similarly, for the ZIF8/3 h sample, the effective convective heat transfer coefficients were $h_{eff} = q_h/A_p/(T_s - T_\infty) = 17.3$ and 17.8 $W \cdot m^{-2} \cdot K^{-1}$ corresponding to $T_s = 90$ and 135°C, respectively (see Figure 5(e)). Minimal differences between samples were observed because the morphologies of ZIF8/1 h and ZIF8/3 h were nearly identical. Notably, for the same sample, h_{eff} should remain fairly constant regardless of the amount of supplied heat because h_{eff} is a material characteristic, which is indeed the case here.

3.4. Single Drop Evaporation and Heat Removal. Figure 6 shows the water contact angles (WCAs) of the bare, ZIF8/1 h, and ZIF8/3 h samples (see first column of Figure 6). Note that the ZIF8 deposition made the substrate slightly more wettable than the bare substrate, although the change in the WCA was not significant. Figure 6 compares photographs of the drop impact phenomena at a substrate temperature of $T_{sub} = 140^{\circ}C$ and a drop release height of $H = 1$ cm. In the bare case, the drop experienced the Leidenfrost effect, and the evaporation of the entire drop with an initial diameter of $D_0 = 4.2$ mm required 3 s. By contrast, the evaporation of water drops of the same size in the ZIF8-coated cases required ~1.6 s. This is because the ZIF8-coated films anchor or pin liquid drops onto the substrate and facilitate droplet spreading after impact. Bubble formation is also apparent within the liquid film spread on the substrate shown in Figure 6. Although the ZIF8-coated films were not highly wettable, liquid pinning and spreading enhanced the evaporation by enhancing or diminishing the Leidenfrost effect.

The water spray-cooling capability of a ZIF8-coated electronic kit was tested, as shown in Figure 7(a). The electronic kit was covered with copper foil on all sides (4 cm × 4 cm × 2 cm), and the top plate was coated with ZIF8. The kit, comprising copper foil, encompassed a ceramic heater at the bottom wall, which had a heating power of $P = 26$ W with a supplied voltage of $V = 20$ V (E3644A, Agilent Corp., USA) and a current of $I = 1.3$ A. The resulting heat flux value at the ceramic heater was $q'' = P/A_p = 1.63$ $W \cdot cm^{-2}$ with the surrounding temperature of $T_\infty = 20^{\circ}C$. This heat flux was dissipated through the five walls of the electronic kit. Most water droplets were sprayed onto the top surface of the kit. Water spray droplets were generated using a water spray bottle with a nozzle diameter of 1 mm. The initial spray injection velocity was estimated to be 0.21 m/s when the volumetric flow rate was 0.167 $ml \cdot s^{-1}$. The volumetric flow rate and spray injection angle were adjusted to focus all injected droplets onto the target (i.e., the top surface of the kit). The spray injection was set to be horizontal, and the injected droplets rapidly slowed as a result of aerodynamic drag and then collapsed onto the

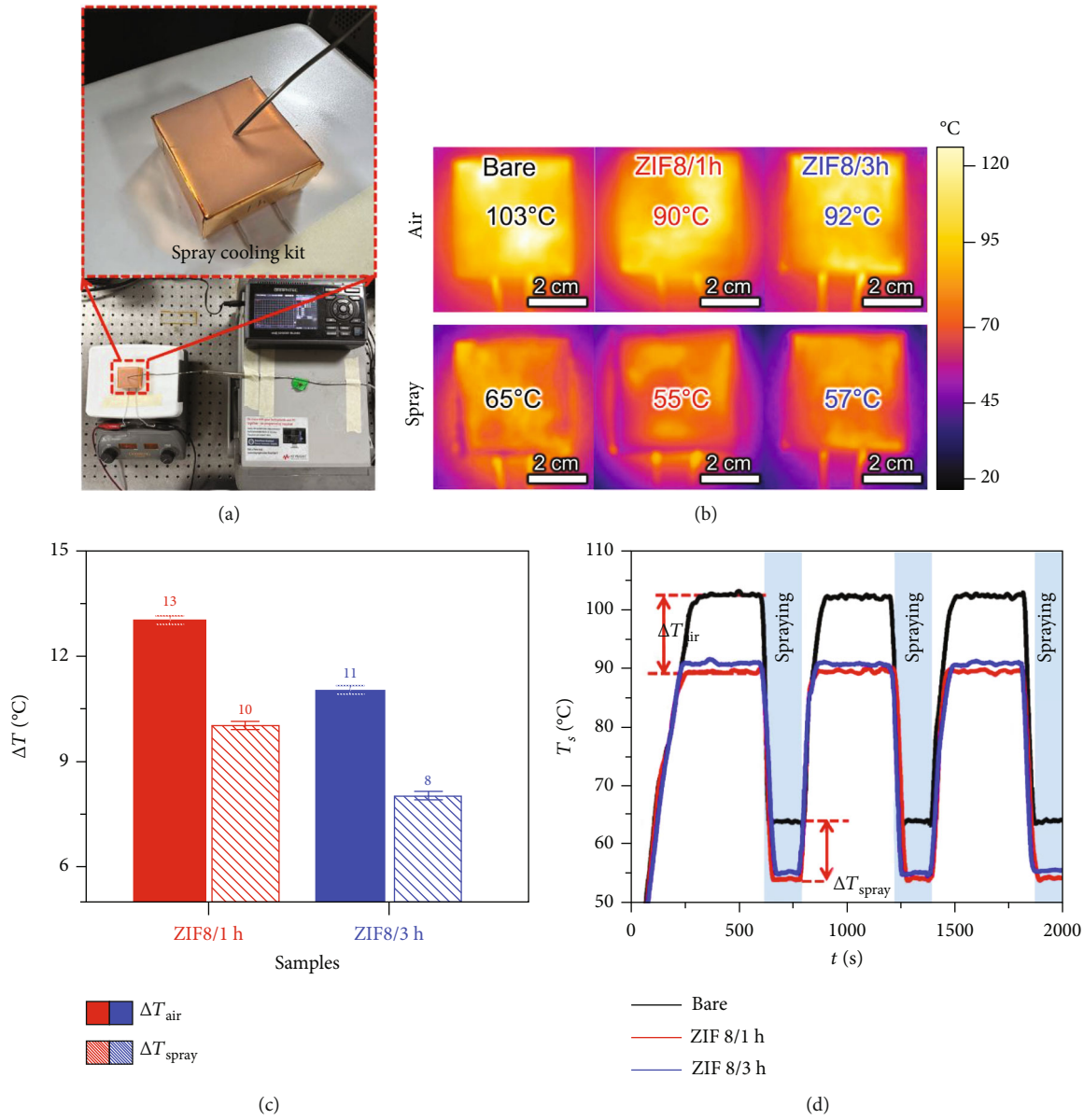

FIGURE 7: (a) Photographs of an electronic kit being cooled via water spraying. (b) Infrared images of the bare, ZIF8/1 h, and ZIF8/3 h cases. (c) Multiple air (ΔT_{air}) and spray (ΔT_{spray}) cooling cycles for the bare, ZIF8/1 h, and ZIF8/3 h cases. (d) Average temperature reduction during air (ΔT_{air}) and spray (ΔT_{spray}) cooling for the three cycles indicated in (c).

electronics kit under gravity. Therefore, the inertial effect of the initial injection was inconsequential, and only the gravitational force affected the free-fall velocity of the droplets. The free-fall velocity was estimated to be 1.4 m·s^{-1} according to $(2gH)^{1/2}$, where g denotes the gravitational acceleration and H is the droplet release height. The duration of the spray-cooling experiment for each case was 30 min, and each sample was subjected to three cycles of heating and cooling. As a result, 10 min was allocated for each cycle, which lasted 7 and 3 min without and with spraying, respectively.

Figure 7(b) shows the infrared images of the bare, ZIF8/1 h, and ZIF8/3 h samples in the air- and spray-cooling scenarios. During natural air cooling, ZIF8/1 h and ZIF8/3 h exhibited temperature drops of $\Delta T_{air} = 13$ and 11°C, respectively, with an error margin of less than 2% (Figure 7(c)). During spray cooling, the coated copper foils resulted in temperature drops of $\Delta T_{air} = 10$ and 8°C (see Figure 7(c)). Thus, these air- and spray-cooling experiments confirmed that the coated copper foils offered better cooling capabilities than the bare copper foil. Figure 7(d) shows the temperature-time plots of the bare, ZIF8/1 h, and ZIF8/3 h samples during the air- and spray-cooling experiments. As most of the injected water droplets were focused on the top surface of the kit, spray cooling resulted in a temperature reduction of $\Delta T_s = 38$°C (i.e., from $T_s = 103$ to 65°C) for the bare case. Similarly, the ZIF8/1 h and ZIF8/3 h cases resulted in a temperature reduction of $\Delta T_s = 35$°C. Thus, the magnitude of the temperature reduction was greater in the bare

case than in the coated case. However, the absolute value of the cooling temperature was 8–10°C lower for the coated cases than that for the bare case. Figures S1c and S1d confirm that the coated ZIF8 layers are mechanically and thermally stable and resilient while exhibiting the same surface temperature (T_s) throughout the duration of 30 min for the air- and spray-cooling cycle tests.

4. Conclusion

Supersonic spraying was used to deposit ZnO particles as a seeding medium for ZIF8 growth via impregnation. The resulting rhombic dodecahedral structure of ZIF8 provided a textured surface for heat transfer enhancement due to the increased surface area. The ZIF8-coated films were placed in a vertical channel (with rising buoyant air or mist flow) to cool the irradiated surfaces. The following summarizes the quantitative data acquired during the cooling tests: the ZIF8-coated films exhibited a temperature reduction in the range of $5.4°C \leq \Delta T_{s,\text{air}} \leq 6.1°C$ and $4.9°C \leq \Delta T_{s,\text{mist}} \leq 5.5°C$ under air- and mist-cooling scenarios, respectively. During plate heating, the ZIF8 films were placed horizontally on a plate heater, and the natural plume rose due to buoyancy during air cooling. The ZIF8-coated cases produced a temperature reduction in the range of $15°C \leq \Delta T_s \leq 16°C$ with respect to the bare case at $T_{s,\text{bare}} = 150°C$. At a lower heating power of $T_{s,\text{bare}} = 100°C$, the temperature reduction range was $10°C \leq \Delta T_s \leq 11°C$. However, we confirmed that the corresponding h_{eff} value remained constant regardless of the heating power because h_{eff} is a unique characteristic of textured surfaces. The percentage increase in h_{eff} from the bare case to the coated cases was 15%-17%. Therefore, the surface area increase resulting from ZIF8 texturing enhanced the cooling capability by 15%–17%. However, the surface area increase was limited due to the growth limit of ZIF8 nanoparticles prepared from this process. Therefore, the convective cooling performance achieved by increasing the surface area was insensitive to the ZIF8 impregnation time from 1 to 3 h.

Nomenclature

A_h: Area of the plate heater
A_p: The projected area of the sample
D_0: An initial diameter of water drop
Gr: Grashof number
g: The acceleration of gravity
H: Drop release height
h_{eff}: The effective convective heat transfer coefficient
h_h: The convective heat transfer coefficient of the heater
k: Thermal conductivity
L: Characteristic length
Nu: Nusselt number
Pr: Prandtl number
q'': Heat flux
q_h: The heat supplied to the plate heater
ΔT: The difference between substrate temperature and atmosphere saturation temperature
T_s: Specimen surface temperature
T_∞: The atmospheric temperature
T_h: The plate heater
T_1: The temperature on the irradiated side outside the channel
Δx: The layer thickness.

Abbreviations

DMF: Dimethylformamide
PAN: Polyacrylonitrile
SWCA: The static water contact angle
ZIF8: Zeolitic imidazolate framework-8.

Greek Symbols

ν: Kinematic viscosity coefficient of fluid.

Data Availability

The data that support the findings of this study are available from the corresponding authors upon reasonable request.

Conflicts of Interest

The authors declared no potential conflicts of interest with respect to the research, authorship and/or publication of this article.

Authors' Contributions

Chanwoo Park, Kwangjin Jang, and Jungwoo Huh contributed equally to this work.

Acknowledgments

This work is supported by the Korea Agency for Infrastructure Technology Advancement (KAIA) grant funded by the Ministry of Land, Infrastructure and Transport (Grant RS-2021-KA163162). This work was supported by the National Research Foundation of Korea (NRF) grant funded by the Korea government (MSIT) NRF-2020R1A5A1018153 and 2022M3J1A106422611. The authors acknowledge King Saud University, Riyadh, Saudi Arabia, for funding this work through Researchers Supporting Project Number (RSP2023R30).

Supplementary Materials

The repeatability results of all cases used in this study are provided in the supplementary materials. Figure S1. Repeatability tests for surface temperature-time plots for the bare, ZIF8/1 h, and ZIF8/3 h cases during (a) air and (b) mist cooling. Repeatable average temperature reduction during air and spray cooling for the three spraying cycles in the (c) fifth and (d) tenth tests. *(Supplementary Materials)*

References

[1] Y. Sun, Z. Guan, H. Gurgenci, J. Wang, P. Dong, and K. Hooman, "Spray cooling system design and optimization for cooling performance enhancement of natural draft dry

cooling tower in concentrated solar power plants," *Energy*, vol. 168, pp. 273–284, 2019.

[2] L.-H. Yang, J.-D. Liang, C.-Y. Hsu, T.-H. Yang, and S.-L. Chen, "Enhanced efficiency of photovoltaic panels by integrating a spray cooling system with shallow geothermal energy heat exchanger," *Renewable Energy*, vol. 134, pp. 970–981, 2019.

[3] S. Lei, Y. Shi, and G. Chen, "Heat-pipe based spray-cooling thermal management system for lithium-ion battery: experimental study and optimization," *International Journal of Heat and Mass Transfer*, vol. 163, article 120494, 2020.

[4] B. Kumar, R. Kumar, and A. Gupta, "Spray cooling of vertical inline horizontal tubes," *Nuclear Engineering and Design*, vol. 407, article 112310, 2023.

[5] F. Tavakkoli, S. Ebrahimi, S. Wang, and K. Vafai, "Analysis of critical thermal issues in 3D integrated circuits," *International Journal of Heat and Mass Transfer*, vol. 97, pp. 337–352, 2016.

[6] H. Tang, Y. Tang, Z. Wan et al., "Review of applications and developments of ultra-thin micro heat pipes for electronic cooling," *Applied Energy*, vol. 223, pp. 383–400, 2018.

[7] S. Zhang, J. Chen, Y. Sun et al., "Experimental study on the thermal performance of a novel ultra-thin aluminum flat heat pipe," *Renewable Energy*, vol. 135, pp. 1133–1143, 2019.

[8] G. Chen, M. Jia, S. Zhang, Y. Tang, and Z. Wan, "Pool boiling enhancement of novel interconnected microchannels with reentrant cavities for high-power electronics cooling," *International Journal of Heat and Mass Transfer*, vol. 156, article 119836, 2020.

[9] C. Wang, L. Hua, H. Yan, B. Li, Y. Tu, and R. Wang, "A thermal management strategy for electronic devices based on moisture sorption-desorption processes," *Joule*, vol. 4, no. 2, pp. 435–447, 2020.

[10] M. Chandrasekar, S. Rajkumar, and D. Valavan, "A review on the thermal regulation techniques for non integrated flat PV modules mounted on building top," *Energy and Buildings*, vol. 86, pp. 692–697, 2015.

[11] A. Luque and S. Hegedus, *Handbook of Photovoltaic Science and Engineering*, John Wiley & Sons, 2010.

[12] T. Kim, C. Park, Y. Kim et al., "Enhancing solar radiant heat transfer using supersonically sprayed rGO/AgNW textured surfaces," *International Journal of Precision Engineering and Manufacturing-Green Technology*, vol. 10, no. 1, pp. 23–33, 2023.

[13] F. Bayrak, H. F. Oztop, and F. Selimefendigil, "Experimental study for the application of different cooling techniques in photovoltaic (PV) panels," *Energy Conversion and Management*, vol. 212, article 112789, 2020.

[14] A. C. Kheirabadi and D. Groulx, "Cooling of server electronics: a design review of existing technology," *Applied Thermal Engineering*, vol. 105, pp. 622–638, 2016.

[15] G. Singh, M. K. Gupta, H. Hegab et al., "Progress for sustainability in the mist assisted cooling techniques: a critical review," *The International Journal of Advanced Manufacturing Technology*, vol. 109, no. 1-2, pp. 345–376, 2020.

[16] X. Meng, L. Meng, Y. Gao, and H. Li, "A comprehensive review on the spray cooling system employed to improve the summer thermal environment: application efficiency, impact factors, and performance improvement," *Building and Environment*, vol. 217, article 109065, 2022.

[17] R. Kandasamy, J. Y. Ho, P. Liu, T. N. Wong, K. C. Toh, and C. Sunshine Jr., "Two-phase spray cooling for high ambient temperature data centers: evaluation of system performance," *Applied Energy*, vol. 305, article 117816, 2022.

[18] Y. Sun, Z. Guan, H. Gurgenci, X. Li, and K. Hooman, "A study on multi-nozzle arrangement for spray cooling system in natural draft dry cooling tower," *Applied Thermal Engineering*, vol. 124, pp. 795–814, 2017.

[19] P. Ding, Y. Liu, W. Li, B. Wang, C. Zhang, and M. Chen, "Numerical investigation on the performance of the combined passive and spray cooling system under nuclear severe accident," *Annals of Nuclear Energy*, vol. 105, pp. 329–345, 2017.

[20] D. H. Lim and S. C. Kim, "Thermal performance of oil spray cooling system for in-wheel motor in electric vehicles," *Applied Thermal Engineering*, vol. 63, no. 2, pp. 577–587, 2014.

[21] J.-X. Wang, Y.-Z. Li, X.-K. Yu, G.-C. Li, and X.-Y. Ji, "Investigation of heat transfer mechanism of low environmental pressure large- space spray cooling for near-space flight systems," *International Journal of Heat and Mass Transfer*, vol. 119, pp. 496–507, 2018.

[22] J.-X. Wang, W. Guo, K. Xiong, and S.-N. Wang, "Review of aerospace-oriented spray cooling technology," *Progress in Aerospace Sciences*, vol. 116, article 100635, 2020.

[23] S. Sinha-Ray and A. L. Yarin, "Drop impact cooling enhancement on nano-textured surfaces. Part I: theory and results of the ground (1 g) experiments," *International Journal of Heat and Mass Transfer*, vol. 70, pp. 1095–1106, 2014.

[24] S. Sinha-Ray, S. Sinha-Ray, A. L. Yarin, C. M. Weickgenannt, J. Emmert, and C. Tropea, "Drop impact cooling enhancement on nano-textured surfaces. Part II: results of the parabolic flight experiments [zero gravity (0g) and supergravity (1.8g)]," *International Journal of Heat and Mass Transfer*, vol. 70, pp. 1107–1114, 2014.

[25] S. An, H. S. Jo, S. S. Al-Deyab, A. L. Yarin, and S. S. Yoon, "Nano-textured copper oxide nanofibers for efficient air cooling," *Journal of Applied Physics*, vol. 119, no. 6, article 065306, 2016.

[26] T.-G. Kim, C.-W. Park, D.-Y. Woo, J. Choi, and S. S. Yoon, "Efficient heat spreader using supersonically sprayed graphene and silver nanowire," *Applied Thermal Engineering*, vol. 165, article 114572, 2020.

[27] T.-G. Kim, C.-W. Park, Y.-i. Kim, A. Aldalbahi, M. Rahaman, and S. S. Yoon, "Supersonically sprayed carbon nanotubes and silver nanowires as efficient heat spreaders and cooling films," *Journal of Applied Physics*, vol. 127, no. 10, article 105105, 2020.

[28] S. Sinha-Ray, Y. Zhang, and A. L. Yarin, "Thorny devil nano-textured fibers: the way to cooling rates on the order of 1 kW/cm^2," *Langmuir*, vol. 27, no. 1, pp. 215–226, 2011.

[29] H. Yoon, M.-w. Kim, H. Kim et al., "Efficient heat removal via thorny devil nanofiber, silver nanowire, and graphene nano-textured surfaces," *International Journal of Heat and Mass Transfer*, vol. 101, pp. 198–204, 2016.

[30] M.-W. Kim, T. G. Kim, H. S. Jo et al., "Nano-textured surfaces using hybrid micro- and nano-materials for efficient water cooling," *International Journal of Heat and Mass Transfer*, vol. 123, pp. 1120–1127, 2018.

[31] T. Kim, S. An, C. Park, J. Choi, A. L. Yarin, and S. S. Yoon, "Flexible heat-spreading and air-cooling films using nickel-electroplated nanotextured fibers," *Chemical Engineering Science*, vol. 227, article 115951, 2020.

[32] T. Kim, C. Park, M. Kim, S. An, and S. S. Yoon, "Highly nano-textured nickel-electroplated bismuth vanadate micropillars

for hotspot removal via air- and spray-cooling," *International Journal of Heat and Mass Transfer*, vol. 156, article 119731, 2020.

[33] C. Zhang and W. J. Koros, "Zeolitic imidazolate framework-enabled membranes: challenges and opportunities," *Journal of Physical Chemistry Letters*, vol. 6, no. 19, pp. 3841–3849, 2015.

[34] K. S. Park, Z. Ni, A. P. Côté et al., "Exceptional chemical and thermal stability of zeolitic imidazolate frameworks," *Proceedings of the National Academy of Sciences*, vol. 103, no. 27, pp. 10186–10191, 2006.

[35] Q. Ma, G. Li, X. Liu, Z. Wang, Z. Song, and H. Wang, "Zeolitic imidazolate framework-8 film coated stainless steel meshes for highly efficient oil/water separation," *Chemical Communications*, vol. 54, no. 44, pp. 5530–5533, 2018.

[36] M. S. Mirqasemi, M. Homayoonfal, and M. Rezakazemi, "Zeolitic imidazolate framework membranes for gas and water purification," *Environmental Chemistry Letters*, vol. 18, no. 1, pp. 1–52, 2020.

[37] Y. Liu, H. Pang, X. Wang et al., "Zeolitic imidazolate framework-based nanomaterials for the capture of heavy metal ions and radionuclides: a review," *Chemical Engineering Journal*, vol. 406, article 127139, 2021.

[38] Z. Mo, D. Z. Tai, H. Zhang, and A. Shahab, "A comprehensive review on the adsorption of heavy metals by zeolite imidazole framework (ZIF-8) based nanocomposite in water," *Chemical Engineering Journal*, vol. 443, article 136320, 2022.

[39] A. Phan, C. J. Doonan, F. J. Uribe-Romo, C. B. Knobler, M. O'Keeffe, and O. M. Yaghi, "Synthesis, structure, and carbon dioxide capture properties of zeolitic imidazolate frameworks," *Accounts of Chemical Research*, vol. 43, no. 1, pp. 58–67, 2010.

[40] Z. R. Herm, E. D. Bloch, and J. R. Long, "Hydrocarbon separations in metal–organic frameworks," *Chemistry of Materials*, vol. 26, no. 1, pp. 323–338, 2014.

[41] W. Morris, B. Leung, H. Furukawa et al., "A combined experimental– computational investigation of carbon dioxide capture in a series of isoreticular zeolitic imidazolate frameworks," *Journal of the American Chemical Society*, vol. 132, no. 32, pp. 11006–11008, 2010.

[42] X. Xu, H. Wang, J. Liu, and H. Yan, "The applications of zeolitic imidazolate framework-8 in electrical energy storage devices: a review," *Journal of Materials Science: Materials in Electronics*, vol. 28, no. 11, pp. 7532–7543, 2017.

[43] S. Feng, X. Zhang, D. Shi, and Z. Wang, "Zeolitic imidazolate framework-8 (ZIF-8) for drug delivery: a critical review," *Frontiers of Chemical Science and Engineering*, vol. 15, no. 2, pp. 221–237, 2021.

[44] V. Hoseinpour and Z. Shariatinia, "Applications of zeolitic imidazolate framework-8 (ZIF-8) in bone tissue engineering: a review," *Tissue & Cell*, vol. 72, article 101588, 2021.

[45] D. Givirovskaia, G. Givirovskiy, M. Haapakoski et al., "Modification of face masks with zeolite imidazolate framework-8: a tool for hindering the spread of COVID-19 infection," *Microporous and Mesoporous Materials*, vol. 334, article 111760, 2022.

[46] M. He, J. Yao, L. Li, Z. Zhong, F. Chen, and H. Wang, "Aqueous solution synthesis of ZIF-8 films on a porous nylon substrate by contra-diffusion method," *Microporous and Mesoporous Materials*, vol. 179, pp. 10–16, 2013.

[47] D.-Y. Kim, B. N. Joshi, J.-G. Lee et al., "Supersonic cold spraying for zeolitic metal-organic framework films," *Chemical Engineering Journal*, vol. 295, pp. 49–56, 2016.

[48] S. R. Venna, J. B. Jasinski, and M. A. Carreon, "Structural evolution of zeolitic imidazolate framework-8," *Journal of the American Chemical Society*, vol. 132, no. 51, pp. 18030–18033, 2010.

[49] A. Schejn, L. Balan, V. Falk, L. Aranda, G. Medjahdi, and R. Schneider, "Controlling ZIF-8 nano- and microcrystal formation and reactivity through zinc salt variations," *CrystEngComm*, vol. 16, no. 21, pp. 4493–4500, 2014.

[50] C. Park, B. Y. Kim, Y.-I. Kim, Y. T. Kang, and S. S. Yoon, "Pool boiling performance of TiO_2 superhydrophilic and Teflon superhydrophobic surfaces on evenly deposited copper frustums," *Case Studies in Thermal Engineering*, vol. 41, article 102581, 2023.

[51] S. Talam, S. R. Karumuri, and N. Gunnam, "Synthesis, characterization, and spectroscopic properties of ZnO nanoparticles," *ISRN Nanotechnology*, vol. 2012, Article ID 372505, 6 pages, 2012.

[52] W. Muhammad, N. Ullah, M. Haroon, and B. H. Abbasi, "Optical, morphological and biological analysis of zinc oxide nanoparticles (ZnO NPs) using Papaver somniferum L," *RSC Advances*, vol. 9, no. 51, pp. 29541–29548, 2019.

[53] C. Li, C. Hu, Y. Zhao et al., "Decoration of graphene network with metal-organic frameworks for enhanced electrochemical capacitive behavior," *Carbon*, vol. 78, pp. 231–242, 2014.

[54] E. Samuel, B. Joshi, M.-W. Kim et al., "Zeolitic imidazolate framework-8 derived zinc oxide/ carbon nanofiber as free-standing electrodes for lithium storage in lithium-ion batteries," *Journal of Power Sources*, vol. 395, pp. 349–357, 2018.

[55] J. Liu, J. He, L. Wang et al., "NiO-PTA supported on ZIF-8 as a highly effective catalyst for hydrocracking of Jatropha oil," *Scientific Reports*, vol. 6, no. 1, article 23667, 2016.

[56] D. Muñoz-Gil and F. M. Figueiredo, "High surface proton conduction in nanostructured ZIF-8," *Nanomaterials*, vol. 9, no. 10, p. 1369, 2019.

[57] J. P. Holman, *Experimental Methods for Engineers*, McGraw-Hill, New York, 2021.